The Journal of Chemical Physics

Quantum HF/DFT-embedding algorithms for electronic structure calculations: Scaling up to complex molecular systems

Cite as: J. Chem. Phys. **154**, 114105 (2021); https://doi.org/10.1063/5.0029536
Submitted: 14 September 2020 . Accepted: 11 February 2021 . Published Online: 15 March 2021

Max Rossmannek, Panagiotis Kl. Barkoutsos, Pauline J. Ollitrault, and Ivano Tavernelli

AIP Publishing

The Journal of Chemical Physics ARTICLE scitation.org/journal/jcp

Quantum HF/DFT-embedding algorithms for electronic structure calculations: Scaling up to complex molecular systems

Cite as: J. Chem. Phys. 154, 114105 (2021); doi: 10.1063/5.0029536
Submitted: 14 September 2020 • Accepted: 11 February 2021 •
Published Online: 15 March 2021

Max Rossmannek,[1,2] Panagiotis Kl. Barkoutsos,[1] Pauline J. Ollitrault,[1,3] and Ivano Tavernelli[1,a)]

AFFILIATIONS

[1]IBM Quantum, IBM Research – Zurich, 8803 Rüschlikon, Switzerland
[2]Department of Chemistry, University of Zurich, Winterthurerstrasse 190, 8057 Zürich, Switzerland
[3]Laboratory of Physical Chemistry, ETH Zurich, 8093 Zürich, Switzerland

[a)]**Author to whom correspondence should be addressed:** ita@zurich.ibm.com

ABSTRACT

In the near future, material and drug design may be aided by quantum computer assisted simulations. These have the potential to target chemical systems intractable by the most powerful classical computers. However, the resources offered by contemporary quantum computers are still limited, restricting the simulations to very simple molecules. In order to rapidly scale up to more interesting molecular systems, we propose the embedding of the quantum electronic structure calculation into a classically computed environment obtained at the Hartree–Fock (HF) or density functional theory (DFT) level of theory. This result is achieved by constructing an effective Hamiltonian that incorporates a mean field potential describing the action of the inactive electrons on a selected Active Space (AS). The ground state of the AS Hamiltonian is then determined by means of the variational quantum eigensolver algorithm. We show that with the proposed HF and DFT embedding schemes, we can obtain significant energy corrections to the reference HF and DFT calculations for a number of simple molecules in their strongly correlated limit (the dissociation regime) as well as for systems of the size of the oxirane molecule.

I. INTRODUCTION

Quantum chemistry simulations allow for the prediction of important chemical processes throughout, for instance, the elucidation of reaction mechanisms by means of the calculation of ground or excited state electronic structure properties.[1] A variety of research and industrial applications such as chemical catalysis, material design, drug discovery, and photo-chemical processes for solar energy conversion, just to name a few,[2,3] could take advantage of these methods. Since the development of the first computers, the research on quantum chemistry has blossomed and a large variety of algorithms have been developed aspiring to achieve more accurate solutions of the Schrödinger equation. However, despite many theoretical and algorithmic advances, the solutions of many interesting and relevant problems in chemistry and physics remain out of reach due to the inherent exponential scaling of the Hilbert space associated with the electronic structure calculations. While several approximate methods have been developed in the past to circumvent this issue, these often break down when considering strongly correlated systems such as transition metal complexes[4] and complicated catalytic processes.[5] In the past decades, quantum computing has emerged as a new potential computational paradigm for the solution of many problems in chemistry and physics for which classical algorithms have an unfavorable scaling. In particular, quantum computing has been shown to be a useful resource in a variety of research areas such as chemistry,[4,6] drug discovery,[7] strongly correlated systems,[8,9] field theory,[10,11] material science,[12] and many others.

Despite these recent advances and the possibility to execute calculations on quantum devices (e.g., Ref. 13), the application of

quantum algorithms is still in its infancy. In fact, most of the research in chemistry relies on hybrid quantum–classical algorithms,[14] which use highly optimized classical (number crunching) functionalities together with quantum algorithms for the representation and optimization of the system wavefunction. The most well known quantum chemistry algorithm that provides the means to leverage state-of-the-art quantum hardware is the Variational Quantum Eigensolver (VQE).[15]

For the representation of the many-body wavefunction in quantum circuits, some of the approaches derived in quantum chemistry can be mapped directly to quantum algorithms. In particular, the Hartree–Fock (HF) method has proven to pose a useful starting point for the mapping of electronic structure problems in the qubit space using the so-called *second quantization* formalism. Among the most commonly used post-HF expansions of the many-electron wavefunction in quantum computing is the Coupled Cluster (CC) *Ansatz*,[16–18] which allows for a systematic and controlled inclusion of higher order configurations starting from the uncorrelated HF Slater determinant. Several quantum implementations of CC have already been introduced in the literature,[15,19–25] including schemes for the optimization of the one-electron molecular basis functions.[9,26] It should also be noted that, in the quantum implementation of CC, the Trotterization leads to a dependence of the results on the ordering of the cluster operators.[25,27] In addition to the classically inspired expansions, pure native quantum representations of the many-electron wavefunctions that can be better optimized for the available quantum hardware platforms have been proposed.[21,28,29] However, some of these wavefunction *Ansätze* can exhibit vanishing small energy gradients, leading to difficulties in the optimization process (i.e., Barren plateaus). To overcome this problem, other CC techniques have been developed, which construct the operators directly in the qubit representation.[30,31] These techniques generally result in significantly shorter circuit depths. The combination of the VQE algorithm with the different wavefunction *Ansätze* showed already interesting results in the calculation of ground[19,28,32–34] and excited state properties[15,35–44] of simple molecules (up to a few atoms). However, this protocol does not allow us to scale to larger systems using the currently available classical simulators of quantum circuits (limited to a maximum of about 50 qubits) or the available quantum computers (also limited to a few tens of qubits). Therefore, in order to leverage the potential advantage of the available quantum algorithm, we explore the possibility of an embedding scheme in which only a portion of the full system is represented by the high-level quantum computing approach, while the rest is treated with an efficient but (necessarily) approximated classical representation of the electronic structure, such as HF or Density Functional Theory (DFT). This embedding approach is of particular relevance when the complex, highly correlated, subsystem can be localized in a well defined subspace of the complete set of one-electron orbitals used to represent the many-electron wavefunction. In this case, an accurate description of the electronic structure is obtained at lower cost in terms of the number of orbitals, namely, $\mathcal{O}(N_{qc}^4)$ for the quantum subsystem (where N_{qc} is the number of orbitals encoded in the quantum circuit) and $\mathcal{O}(N_{env}^2)$ to $\mathcal{O}(N_{env}^3)$ for the environment (where N_{env} is the number of orbitals assigned to the classical processor and $N_{tot} = N_{qc} + N_{env}$); this is to be compared with the $\mathcal{O}(N_{tot}^4)$ scaling when no embedding is used and the total set of orbitals (N_{tot}) is considered for the wavefunction *Ansatz*.

In this work, we propose HF and DFT-based quantum embedding schemes based on the well known notion of an Active Space (AS),[45,46] which defines the set of *active* orbitals described by the quantum algorithm. To this end, we construct an effective Hamiltonian, which incorporates a mean field potential of the *inactive* electrons and, thus, fully replaces the explicit mapping of the corresponding orbitals in the quantum register. The quantum algorithm is therefore restricted to a subset of active orbitals, which, however, feel the presence of the environment through the action of the mean field potential generated by the inactive electrons of the environment. Similar approaches of the HF embedding have been proposed in the literature[47,48] mainly based on Dynamical Mean Field Theory (DMFT)[49] and Density Matrix Embedding Theory (DMET)[50] for the high-level description of the subsystem. The latter aims at a similar HF embedding scheme. However, while the focus of its authors was on the development of a self-consistent HF embedding approach,[51] in this work, we only consider iterative embedding within the framework of DFT. Concerning the DMFT approach, this is based on Green's function techniques and therefore it is not particularly suited for the kind of molecular application of interest to this work. Additionally, during the preparation of this paper, another related approach appeared in the literature.[52] In this case, the authors propose a DFT embedding scheme similar to ours, which however uses a different *Ansatz* to resolve the double counting problem of the correlation terms. Furthermore, they do not update the embedding potential in a self-consistent manner as we do in this work.

This paper is organized as follows: In Sec. II, we outline the theory and the implementation of the proposed AS schemes for quantum electronic structure calculations embedded in HF and DFT. We split the derivation into two parts: one for the HF embedding scheme and the other for the DFT embedding scheme. Section III lists the technical details of our numerical methods. In Sec. IV, we present and discuss results on the dissociation of simple molecular systems, such as water, molecular nitrogen, molecular oxygen, and oxirane obtained with both types of embedding schemes. Section V summarizes and concludes.

II. THEORY

In this work, we propose two embedding schemes for quantum electronic structure algorithms based on HF and Kohn–Sham (KS) DFT Molecular Orbitals (MOs). The subsystem solved by means of the quantum approach [such as quantum Unitary Coupled Cluster Singles and Doubles (q-UCCSD)[1,15,21]] is embedded in the potential generated by the environment (i.e., the remaining electrons), which is computed within the HF or DFT framework. Our solutions are based on the Range-Separation (RS) technique for the two-electron integrals,[53] which allows for a rigorous partitioning of the problem into a subsystem (i.e., the AS) and its environment. If this partitioning is done wisely, we can achieve a good level of accuracy for many properties of interest while significantly reducing the costs of the calculation. Furthermore, in the case of the DFT embedding scheme (which is the main target of this work), we will

extend the algorithm to include the self-consistent optimization of the embedding potential, leading to more accurate energies and densities. In the following, we will call *active* electrons the electrons that are part of the AS, while the remaining ones will be referred to as *inactive*.

A. Hartree–Fock embedding

In this section, we derive the so-called *inactive Fock operator*. The goal of this operator is to embed the quantum computation into a classically computed environment treated at the HF level of theory, through the notion of an AS. While this method is not new and different variants of it have been implemented before in other software packages,[52,54,55] in the following, we summarize the key concepts that are needed for its implementation within the framework of quantum computing in Qiskit.[56] This section also lays down the fundamentals for the implementation of the DFT embedding scheme presented in Sec. II B.

The benefit of this embedding scheme lies in outsourcing the calculation of the inactive electrons to the classical HF driver, while the quantum computation is restricted to the AS. In this way, less qubit resources are necessary to investigate the electronic energy of a molecular system, making the entire calculation much more efficient while keeping a good level of accuracy. Figure 1 depicts the separation of the orbitals into the active and inactive spaces.

The total electronic energy, E, is defined by the expectation value of the system Hamiltonian, $\hat{\mathcal{H}}$,

$$E = \langle \Psi | \hat{\mathcal{H}} | \Psi \rangle = \sum_{pq} h_{pq} D_{pq} + \frac{1}{2} \sum_{pqrs} g_{pqrs} d_{pqrs}, \tag{1}$$

where Ψ is the wavefunction, h_{pq} and g_{pqrs} are the one- and two-electron integrals, respectively, and D and d are the one- and two-particle density matrices.

To achieve the implementation of the HF embedding, we split the one-electron density into an active and inactive part, $D = D^A + D^I$. In the MO basis, the latter simplifies to $D^I_{iq} = 2\delta_{iq}$, where we use Helgaker's index notation[46] in which i, j, k, l denote *inactive*, u, v, x, y denote *active*, and p, q, r, s denote *general* MOs. As shown in Appendix A 1, inserting this into Eq. (1) leads to

$$E = E^I + \sum_{uv} F^I_{uv} D^A_{uv} + \frac{1}{2} \sum_{uvxy} g_{uvxy} d^A_{uvxy}, \tag{2}$$

where we define the *inactive Fock operator*,

$$F^I_{pq} = h_{pq} + \sum_i (2g_{iipq} - g_{iqpi}), \tag{3}$$

and the *inactive energy*,

$$E^I = \sum_j h_{jj} + F^I_{jj} = \frac{1}{2} \sum_{ij} \left(h_{ij} + F^I_{ij}\right) D^I_{ij}. \tag{4}$$

Comparing Eqs. (1) and (2), we observe the following differences. In Eq. (2), the *inactive* Fock operator, F^I, replaces the one-electron integrals, h_{pq}; the *active* one- and two-electron density matrices, D^A and d^A, replace D and d; and the constant energy offset, E^I, is added.

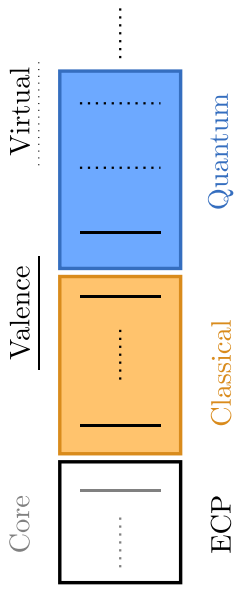

FIG. 1. Separation of the MOs into active and inactive components. The active orbitals (blue box) are mapped onto the qubit space and treated with the q-UCCSD approach, while the inactive ones (orange box) are part of the HF/DFT embedding and are evaluated classically. Effective Core Potentials (ECPs) can be used in replacement of all inactive core electrons (white box) with the aim of reducing the computational cost.

Therefore, the Hamiltonian that we evaluate on the quantum computer (qc) takes the form

$$\hat{\mathcal{H}}_{qc} = \sum_{uv} F^I_{uv} \hat{a}^\dagger_u \hat{a}_v + \sum_{uvxy} g_{uvxy} \hat{a}^\dagger_u \hat{a}^\dagger_v \hat{a}_x \hat{a}_y, \tag{5}$$

where $\hat{a}^\dagger_u$ and $\hat{a}_u$ are the creation and annihilation Fermionic operators (later mapped to the qubit space using the parity transformation[57]). Note that all indices are restricted to the AS, significantly reducing the required quantum resources.

The extension for the unrestricted formalism is obtained in a similar manner and is outlined in Appendix A 2.

B. Density functional theory embedding

In order to extend the embedding to work with DFT, we need to introduce a RS of the two-electron integrals, g_{pqrs}.[53] To this end, we split the two-electron operator, $\hat{g}_{pq}$, into a Long-Range (LR) and a Short-Range (SR) part,

$$\hat{g}_{pq} = \frac{1}{|\hat{r}_p - \hat{r}_q|} = \hat{g}^{\mu,\mathrm{LR}}_{pq} + \hat{g}^{\mu,\mathrm{SR}}_{pq}, \tag{6}$$

where μ is the RS parameter of unit a.u.$^{-1}$. This is necessary in order to avoid a double counting of the correlation terms, which are

present in both DFT and Wave Function Theory (WFT). Since DFT is known to be accurate for SR interactions,[53] we can use it to treat the SR part, while the LR interactions are calculated with WFT.

Our derivation of the following equations follows that of Hedegård *et al.*[58] closely. Additionally, we provide our detailed derivations in Appendix B.

With the RS of the two-electron integrals in place, we can split the total electronic energy into two terms,

$$E = E^{\mu,\mathrm{LR}}_{\mathrm{WFT}} + E^{\mu,\mathrm{SR}}_{\mathrm{coul+xc,DFT}}. \tag{7}$$

Note that Eq. (7) provides an *adiabatic connection* between the pure DFT and the pure WFT solutions through the coupling parameter, μ. However, in order to simplify the notation, we drop the superscript μ since it is anyways implied by the separation into LR and SR.

Analogous to Sec. II A, we can introduce an AS in the WFT part,

$$E = E^{I,\mathrm{LR}}_{\mathrm{WFT}} + E^{A,\mathrm{LR}}_{\mathrm{WFT}} + E^{\mathrm{SR}}_{\mathrm{coul+xc,DFT}}. \tag{8}$$

Note that the difference between Eqs. (2) and (8) is that WFT only treats the LR part. Thus, the *inactive Fock operator*, defined in Eq. (3), becomes

$$F^{I,\mathrm{LR}}_{pq} = h_{pq} + \sum_i \left(2g^{\mathrm{LR}}_{iipq} - g^{\mathrm{LR}}_{iqpi}\right). \tag{9}$$

In order to properly combine the SR-DFT and LR-WFT calculations, we need to handle the non-linearity of $E^{\mathrm{SR}}_{\mathrm{coul+xc,DFT}} = E^{\mathrm{SR}}_{\mathrm{coul+xc}}$ with respect to the electronic density, ρ,

$$E^{\mathrm{SR}}_{\mathrm{coul+xc}}[\rho + \Delta\rho] \neq E^{\mathrm{SR}}_{\mathrm{coul+xc}}[\rho] + E^{\mathrm{SR}}_{\mathrm{coul+xc}}[\Delta\rho], \tag{10}$$

where $\Delta\rho$ is the correction to the density obtained from the WFT calculation. However, a linear approximation can be obtained with the following replacement:

$$E^{\mathrm{SR}}_{\mathrm{coul+xc}}[\rho + \Delta\rho] - E^{\mathrm{SR}}_{\mathrm{coul+xc}}[\rho] \approx \int \frac{\delta E^{\mathrm{SR}}_{\mathrm{coul+xc}}}{\delta\rho(\vec{r})}[\rho]\Delta\rho(\vec{r})\mathrm{d}\vec{r}. \tag{11}$$

The right-hand side of Eq. (11) can then be expressed in terms of the *Coulomb* integrals,

$$j^{\mathrm{SR}}_{pq} = \left\langle \phi_p \middle| \frac{\delta E^{\mathrm{SR}}_{\mathrm{coul}}}{\delta\rho(\vec{r})}[\rho] \middle| \phi_q \right\rangle = \sum_{rs} g^{\mathrm{SR}}_{pqrs} D_{rs}, \tag{12a}$$

and the *exchange* integrals,

$$v^{\mathrm{SR}}_{\mathrm{xc},pq} = \left\langle \phi_p \middle| \frac{\delta E^{\mathrm{SR}}_{\mathrm{xc}}}{\delta\rho(\vec{r})}[\rho] \middle| \phi_q \right\rangle = v^{\mathrm{SR}}_{\mathrm{xc},pq}[\rho], \tag{12b}$$

as

$$\int \frac{\delta E^{\mathrm{SR}}_{\mathrm{coul+xc}}}{\delta\rho(\vec{r})}[\rho]\Delta\rho(\vec{r})\mathrm{d}\vec{r} = \sum_{pq}\left(j^{\mathrm{SR}}_{pq} + v^{\mathrm{SR}}_{\mathrm{xc},pq}\right)\Delta D_{pq}. \tag{13}$$

Because of the non-linearity of Eq. (12b), the density needs to be updated in an iterative, self-consistent manner. Therefore, we define the density and the density matrix at the iteration step i as

$$\rho^{(i+1)} = \rho^{(i)} + \Delta\rho^{(i)}, \tag{14a}$$

$$D^{(i+1)}_{pq} = D^{(i)}_{pq} + \Delta D^{(i)}_{pq}. \tag{14b}$$

This leads to the final form of the total electronic energy,

$$\begin{aligned} E =& \frac{1}{2}\sum_{ij}\left(h_{ij} + F^{I,\mathrm{LR}}_{ij}\right)D^I_{ij} \\ &+ E^{\mathrm{SR}}_{\mathrm{xc}}\left[\rho^{(i)}\right] + \frac{1}{2}\sum_{ij} j^{I,\mathrm{SR}}_{ij} D^I_{ij} \\ &- \sum_{uv}\left[\left(\frac{1}{2}j^{A,(i),\mathrm{SR}}_{uv} + v^{\mathrm{SR}}_{\mathrm{xc},uv}\left[\rho^{(i)}\right]\right)D^{A,(i)}_{uv}\right. \\ &\left. - \left(F^{I,\mathrm{LR}}_{uv} + j^{I,\mathrm{SR}}_{uv} + j^{A,(i),\mathrm{SR}}_{uv} + v^{\mathrm{SR}}_{\mathrm{xc},uv}\left[\rho^{(i)}\right]\right)D^{A,(i+1)}_{uv}\right] \\ &+ \frac{1}{2}\sum_{uvxy} g^{\mathrm{LR}}_{uvxy} d^{A,(i+1)}_{uvxy}, \end{aligned} \tag{15}$$

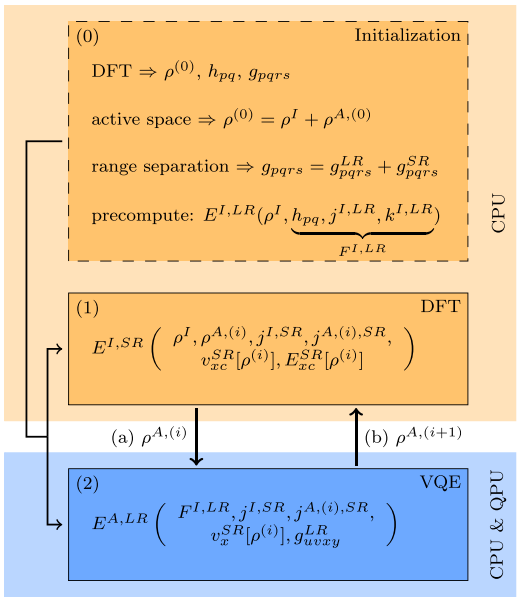

FIG. 2. Illustration of the DFT embedding scheme. During initialization (0), a DFT calculation of the full system is performed using a classical code, providing the initial density, $\rho^{(0)}$, and the one- and two-electron integrals, h_{pq} and g_{pqrs}. The density is then split into inactive, *I*, and active parts, *A*; and the two-electron integrals are separated into long-range, *LR*, and short-range, *SR*, components. In step (1), the inactive SR energy contribution is calculated at the DFT level of theory. The resulting "active" density component (a) is used in step (2) to initialize the VQE optimization. This returns the active LR energy contribution and the updated electronic density, which is used as a new input for the DFT calculation, (b). Steps (1) and (2) are repeated until convergence.

where we have ordered the terms such that the top line contains all contributions, which remain constant for the duration of the whole iterative procedure, the second and third lines correspond to the SR-DFT, and the remaining lines correspond to the LR-WFT energy terms, respectively.

Figure 2 summarizes the implementation of this DFT embedding scheme. The initialization step includes all the pre-calculations and the computation of the constant *inactive* LR energy contribution [first line of Eq. (15)]. The resulting energy terms of steps (1) and (2) in Fig. 2 correspond to lines two and three, and four and five of Eq. (15), respectively. These two calculations iterate, upon exchanging the active electronic density, ρ^A, until the total electronic energy reaches convergence.

III. NUMERICAL METHODS

The HF and DFT embedding schemes have been implemented in the development version 0.8 of Qiskit Aqua Chemistry. The source code will be made available in the Github repository.[59] For the classical computing backend, we choose PySCF[60] since it allows quick prototyping within Python, the same programming language used for Qiskit.

All the results presented hereafter are obtained by means of diagonalizing the Hamiltonian with the `NumPyEigensolver` algorithm, as implemented in Qiskit. In the case of the non-iterative HF embedding scheme, we also run VQE simulations with the `statevector` backend.[59] This backend implements an exact, i.e., noiseless, simulation of the quantum circuit and, thus, is expected to converge to the same result as the `NumPyEigensolver` approach when a suitable wavefunction *Ansatz* is chosen.

A. Hartree–Fock embedding

In all simulations using the HF embedding, we use the parity fermion-to-qubit mapping[57] and the q-UCCSD Ansatz[21] for the representation of the electronic wavefunction. In Qiskit, the q-UCCSD *Ansatz* is implemented in a well-defined manner whose details are outlined in Ref. 21 and Appendix C. Furthermore, qubits are tapered off[61] in order to maximally reduce the computational costs. The classical optimizer L-BFGS-B[62] is used for the optimization of the VQE parameters.

B. Density functional theory embedding

In all DFT embedding applications, we use the RS-XCF (Range-Separated Exchange-Correlation Functional) `ldaerf` scheme,[63,64] as implemented in the xcfun library[65] for the separation of the LDA (Local Density Approximation) functional into its short and long range components (see Sec. II B). This approach achieves the splitting of the two-electron integrals by means of the error function, which is a common approach in RS-DFT.[53,66,67] The use of the LDA functional is solely motivated by the current technical limitations of the PySCF code. Future extensions to allow the use of arbitrary DFT functionals are under investigation. Nonetheless, the proposed scheme is fully independent from the nature of the selected functional and all applications presented in the following should be considered as proof-of-principle demonstrations extendable to any type of DFT functional.

In all applications, we selected the STO-3G basis set, which enabled the calculation of the exact reference curves with full CI (FCI). Furthermore, the optimal value of the range-separation parameter, μ, was selected case-by-case by scanning the interval 0.01–500 and finally picking the value that gives the lowest energy (see the supplementary material for more details).

IV. RESULTS AND DISCUSSION

In this section, we present results on the dissociation of simple molecular systems of increasing size, namely, molecular nitrogen, molecular oxygen, water, and oxirane using the proposed HF and DFT embedding schemes (see Secs. II A and II B, respectively). To enable the comparison with exact results obtained with FCI, we limited our calculations to the relatively small basis set STO-3G. The results obtained with both embedding schemes are compared with standard HF and DFT calculations as well as with other commonly used, correlated, post-HF solutions such as Coupled Cluster Singles and Doubles (CCSD) and Complete Active Space Self-Consistent Field (CASSCF). In particular, we demonstrate that even within the embedding approximation, the quantum CC algorithm can solve some pathologies of classical CCSD in the strongly correlated regime, such as the dissociation of N_2 and O_2. Finally, with the study of oxirane, we show how the proposed embedding schemes can extend the use of quantum algorithms to molecular sizes that would exceed the capabilities of state-of-the-art quantum computers.

A. A benchmark system: Water

We start with the investigation of the AS of water, analyzing the dependence of the energy on the number of molecular orbitals and electrons included in the quantum description. Standard post-HF methods such as Complete Active Space Configuration Interaction (CASCI) and CASSCF as implemented in PySCF[60] are used to benchmark the HF embedding scheme. A study on the effect of the size of the basis set from STO-3G[68] to 6-31G*[69] and cc-pVTZ[70] is given in the supplementary material (Figs. S1 and S2). In the following, we restrict our calculations to the STO-3G basis. Finally, we apply both HF and DFT embedding approaches to the study of the symmetric double-proton dissociation, focusing our attention on the dissociation limit, where strong correlation effects become important.

1. General properties of active-space embedding techniques

Figure 3 summarizes the main results obtained for water in the STO-3G basis. In general, the ground state energies obtained with HF embedding (blue triangles in Fig. 3) are in qualitatively good agreement with the classical CASCI results[60] (orange crosses). The CASSCF[60] energy values (green circles) are consistently lower (or equal) than the CASCI ones since the former also includes the optimization of the orbital coefficients, which are kept fixed in CASCI. More interestingly, all statevector-based VQE calculations using the q-UCCSD *Ansatz* (brown pentagons in Fig. 3) also converge to the exact solutions.

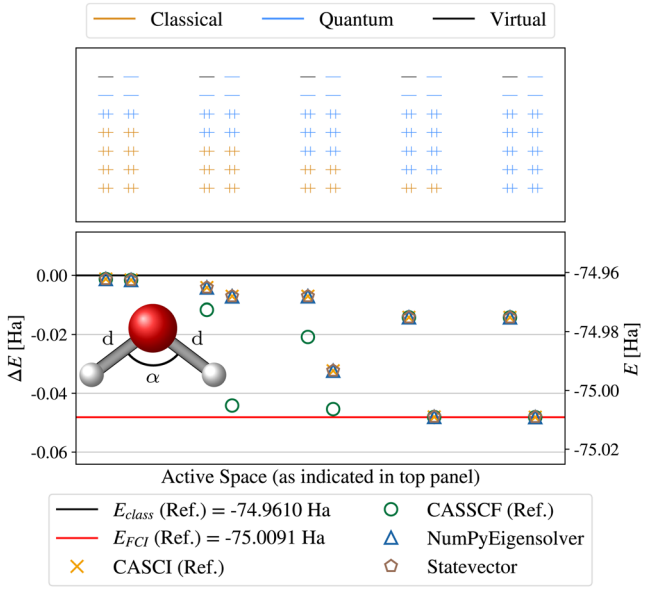

FIG. 3. Electronic structure energies (in Hartree) of a water molecule obtained with the HF embedding scheme for different choices of the AS, which are reported in the upper panel. We report absolute (right axis) and relative energies with respect to HF (left axis). The coloring follows the same scheme used in Figs. 1 and 2: orange for the inactive HF orbitals that define the embedding, blue for the orbitals belonging to the AS, and black for the remaining virtual ones. The classical HF reference (black, solid) is obtained with RHF in the STO-3G basis. As a reference, we also show the results obtained with FCI, CASCI, and CASSCF.

It is worth mentioning that the choice of the AS has a strong, and not always predictable, effect on the outcome. In particular, it is hard to predict *a priori* the optimal AS that maximizes the performance of the embedding calculation.[71,72] In the absence of a systematic procedure, we can explore all possible AS configurations, as shown in Fig. 3, for the case of water in the STO-3G basis set. However, this procedure is only possible for relatively small systems, while it becomes impractical in the most general cases (see, for instance, the additional results in the supplementary material, Figs. S3–S5), leading to a large degree of uncertainty in the application of the embedding approach. On the other hand, recently, we witnessed the development of new numerical techniques, which aim at automatizing the selection of the optimal AS in molecular systems.[33,72–75] The combination of these approaches with our embedding scheme goes however beyond the scope of this work and will become the subject of future investigations.

2. The double-dissociation of water

In this section, we present the symmetric dissociation profile of a water molecule at fixed H–O–H angle of $\alpha = 105.4^\circ$ in the STO-3G basis set using different approaches. For the DFT embedding scheme outlined in Sec. III B, we swept over the range-separation parameter, μ, and found the optimal value for this system to be $\mu_{opt} = 7.0$. These results are reported in Fig. S6 of the supplementary material together with a sketch of the KS-MOs (see Fig. S10).

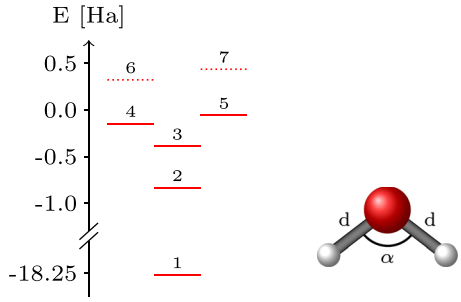

FIG. 4. Energy diagram of the KS-MOs of H_2O in the STO-3G basis. The solid lines correspond to occupied MOs, while the dotted lines represent virtual ones.

Figure 4 depicts these orbitals in an energy diagram. Note that we do not display properly the HF-MOs, but their difference to the shown KS-MOs is minor.

Figure 5 depicts the dissociation curves from $d = 0.5$ Å up to $d = 2.0$ Å, as computed by the proposed DFT- and HF embedding schemes for a selection of ASs. As a comparison, we also show the corresponding profiles computed with CCSD and FCI (computed with PySCF). In general, increasingly larger ASs provide results in closer agreement with the exact solution, as given by FCI even though, as mentioned in Subsection IV A 1, the optimal choice of AS cannot be determined *a priori*.[71,72] This becomes more evident looking at the lower panels of Fig. 5 where we plot the energy differences with respect to the exact value. In addition, note that the DFT embedding scheme is not variational in contrast to HF-based embedding methods.

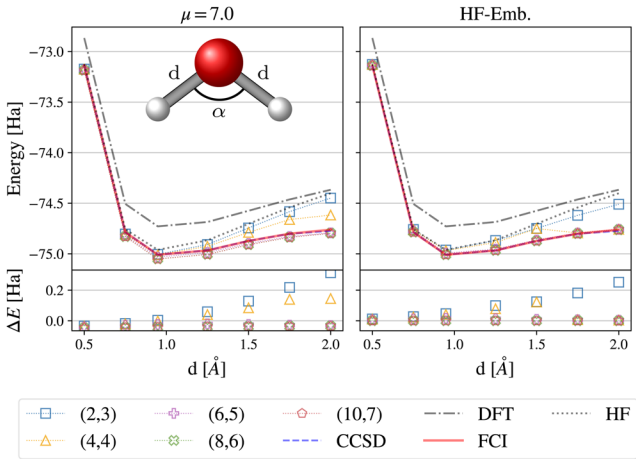

FIG. 5. (Upper panels) Symmetric dissociation profiles of a water molecule at a fixed H–O–H angle ($\alpha = 105.4^\circ$) in the STO-3G basis set. The left panel reports the energies obtained with the DFT embedding scheme at $\mu = 7.0$, while the right panel shows the same curves obtained with the HF embedding scheme, respectively. The size of the ASs is reported in the legend with the format: (number of electrons, number of orbitals). The HF (gray, dotted), DFT (gray, dashed-dotted) (LDA/VWN XCF), CCSD (blue, dashed), and FCI (red, solid) references were computed with PySCF. (Lower panels) Energy differences with respect to the exact FCI reference.

Table I reports dissociation energies and non-parallelity errors (NPEs) for the different methods. The NPE is defined as the difference between the maximum and minimum error over the entire energy profile evaluated with respect to the exact calculation.[76] For brevity, we only report a selection of ASs, while the complete set of calculations can be found in Table S1 of the supplementary material. While all HF embedding calculations lead to better dissociation energies than standard HF (ΔE_{HF} = 559.7 mHa), DFT embedding with CAS(2, 3) and CAS(4, 4) performs worse than standard DFT (ΔE_{DFT} = 361.7 mHa). With the exclusion of these last two cases, we observe a systematic and significant improvement of all results as the size of the AS increases. In particular, the HF embedding can provide nearly exact results (ΔE_{FCI} = 247.1 mHa) with CAS(8, 6) and CAS(10, 7), which is not a surprise as the latter corresponds to the FCI calculation. On the other hand, we observe that the DFT embedding cannot reach the same accuracy even with the larger AS. This is due to the nature of the LDA-DFT-orbitals, which, by definition, cannot reproduce the FCI result based on HF orbitals. However, in the case of large molecular systems with hundreds of electrons, the DFT embedding will become the only viable option for a correct description of a molecular embedding potential.

Additional insights on the accuracy of the different embedding schemes can also be gained from the analysis of the NPE results. The values that show an improvement compared to the standard HF and DFT calculations are highlighted in bold. In agreement with the observations based on the dissociation energies and on the profiles shown in Fig. 5, we observe a systematic improvement of the quality of the results by increasing the AS [from CAS(6, 5) to CAS(10, 7)]. Even though the above results were obtained with μ values selected through energy minimization, other techniques exist for this purpose,[67] which could lead to a further improvement of our results.

It is worth mentioning that this behavior cannot be generalized to all situations. In fact, as it will also become evident for the other systems, increasing the number of electrons while keeping the number of orbitals constant implies a reduction of the number of virtual orbitals available for the excitations. In addition, the ordering of the molecular orbitals may change upon stretching, shifting in and out new orbitals from the selected AS, and leading to sudden changes in the energy profiles. Once more, we observe that the HF embedding in general produces better estimates than the DFT embedding due to the fact that we use HF orbitals for the reference FCI calculation. In addition, in general, the HF embedding improves upon the initial HF-estimate more than the DFT embedding does. Finally, the quality of the CASSCF results suggests that future extensions to incorporate an iterative optimization of the orbitals could yield further improvements, especially in the case of small ASs.

TABLE I. Dissociation energies, ΔE, and NPE values for the symmetric double-stretch of water. ΔE are computed as the difference between the energies at equilibrium, d = 0.948 Å, and at d = 2.0 Å. The NPE values are given within parentheses. The results for HF, DFT, FCI, and CCSD are ΔE_{HF} = 559.7 (347.3) mHa, ΔE_{DFT} = 361.7 (122.8) mHa, ΔE_{FCI} = 247.1 (0.0) mHa, and ΔE_{CCSD} = 236.0 (12.0) mHa, respectively. Situations that show an improvement of the NPE compared to standard HF and DFT are highlighted in bold.

CAS	μ = 7.0 (NPE)	HF-Emb. (NPE)	CASSCF (NPE)
(2, 3)	557.0 (347.2)	452.5 (239.7)	368.6 (165.0)
(4, 4)	393.4 (181.1)	210.5 (118.3)	244.0 (117.4)
(6, 5)	**239.6 (20.3)**	**235.5 (11.6)**	**245.0 (2.1)**
(8, 6)	**253.7 (11.7)**	**247.1 (0.1)**	**247.1 (0.1)**
(10, 7)	**254.1 (12.2)**	**247.1 (0.0)**	**247.1 (0.0)**

B. The dissociation of molecular nitrogen and oxygen

As a second example, we investigate the dissociation of molecular nitrogen and oxygen, which show strong correlation character at large distances. In fact, it is well known in the literature that for both systems CCSD fails to produce the correct dissociation profile (cf. Ref. 9 and the references therein).

For the determination of the range-separation parameter μ, we follow the procedure outlined in Sec. III B. The optimal values were found to be $\mu_{opt}[N_2]$ = 7.0 and $\mu_{opt}[O_2]$ = 8.0, respectively (see Figs. S7 and S8 of the supplementary material). A sketch of the KS molecular orbitals is also given in the supplementary material (Figs. S11 and S12). Figures 6 and 7 depict energy diagrams for the KS-MOs of nitrogen and oxygen, respectively, and provide a useful indication of the relative energies of the orbitals involved in our choices of AS. In Figs. 8 and 9, we report the dissociation profiles between d = 1.0 Å and d = 3.0 Å computed with the different AS sizes together with the standard HF, DFT, and CCSD results and the reference FCI calculation. In the case of N_2, the curve produced with CCSD is qualitatively wrong, showing an unphysical drop in energy as the distance increases beyond about d = 2 Å. This result is in agreement with the results reported in Ref. 9. The CCSD situation of O_2 is slightly better, even though the deviation from the exact FCI curve is sizable along the entire dissociation profile. Concerning the standard HF and DFT calculations, we also observe large discrepancies compared to the exact curve in both systems, with the first one showing large overestimation of the dissociation energies due to the complete neglect of the correlation energy.

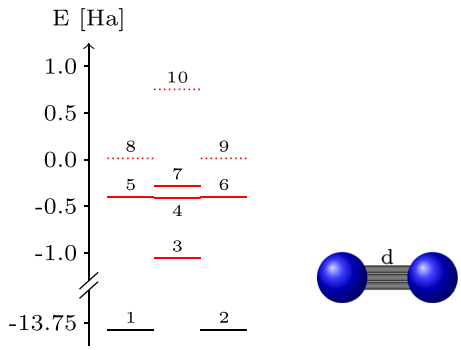

FIG. 6. Energy diagram of the KS-MOs of N_2 in the STO-3G basis. The solid lines correspond to occupied MOs, while the dotted lines represent virtual ones. In *red* are the orbitals involved in at least one of the ASs considered.

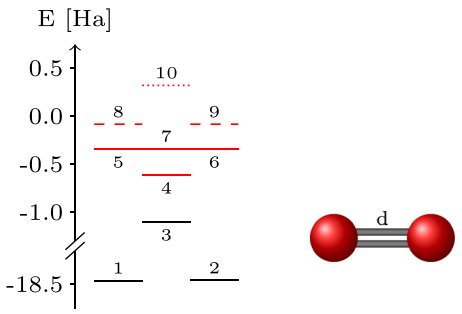

FIG. 7. Energy diagram of the KS-α-SOs of O_2 in the STO-3G basis. The solid lines correspond to energy levels for which both α and β SO are occupied, the dashed lines are singly occupied, and the dotted lines represent virtual orbitals. In *red* are the orbitals involved in at least one of the ASs considered.

As for the case of water, increasing the size of the AS in the HF embedding scheme, we observe a gradual increase in the accuracy of the calculations, reaching for the larger AS [CAS(6, 6) and CAS(8, 7) in the case of N_2 and CAS(8, 6) and CAS(10, 7) in the case of O_2] results within a few mHa from the reference curve. We also observe for O_2 some discontinuities in the dissociation profiles at about $d = 2$ Å in both CAS(2, 3) and CAS(4, 4) calculations. This effect is due to a swap in the ordering of the KS orbitals induced by the stretching of the bond, which causes an abrupt change in the composition of the AS. This has a particular impact on the energy in the case of small AS composed of only a few KS orbitals around the Fermi level.

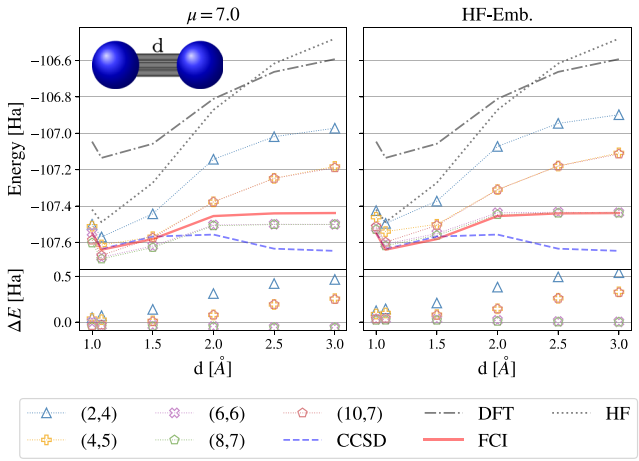

FIG. 8. (Upper panels) Dissociation profiles of a nitrogen molecule in the STO-3G basis set. The left panel reports the energies obtained with the DFT embedding scheme at $\mu = 7.0$, while the right panel shows the same curves obtained with the HF embedding scheme, respectively. The size of the ASs is reported in the legend with the format: (number of electrons, number of orbitals). The HF (gray, dotted), DFT (gray, dashed-dotted) (LDA/VWN XCF), CCSD (blue, dashed), and FCI (red, solid) references were computed with PySCF. (Lower panels) Energy differences with respect to the exact FCI reference.

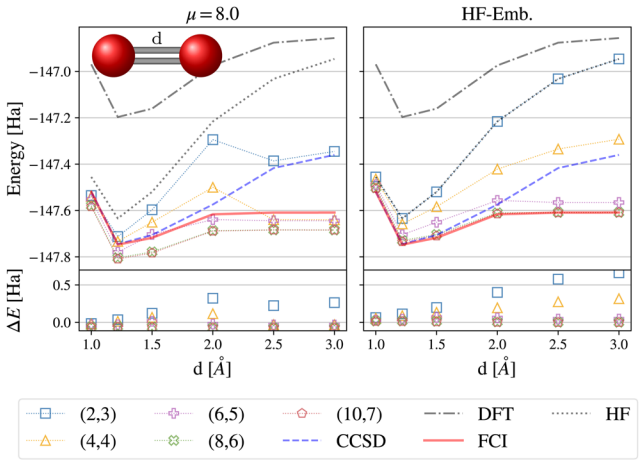

FIG. 9. (Upper panels) Dissociation profiles of an oxygen molecule in the STO-3G basis set. The left panel reports the energies obtained with the DFT embedding scheme at $\mu = 8.0$, while the right panel shows the same curves obtained with the HF embedding scheme, respectively. The size of the ASs is reported in the legend with the format: (number of electrons, number of orbitals). The HF (gray, dotted), DFT (gray, dashed-dotted) (LDA/VWN XCF), CCSD (blue, dashed), and FCI (red, solid) references were computed with PySCF. (Lower panels) Energy differences with respect to the exact FCI reference.

In Tables II and III, we summarize the results of the N_2 and O_2 calculations reporting the values of the dissociation energies and NPEs for the different AS sizes, together with the CASSCF results. These results confirm our previous observations, which point toward a systematic increase in the quality of the results with the increase in the AS size. However, we need to stress once more that due to the small size of the basis set, the different number of virtual orbitals in CAS(n, m) when the number of electrons n increases at fixed value of m, and the issue with the orbital crossing mentioned above, we cannot always expect a monotonic decrease in the error as a function of parameters n and m. As already mentioned above, in many cases, a careful analysis of the orbitals included in the AS and their occupancy is required in order to achieve the desired accuracy.

TABLE II. Dissociation energies, ΔE, and NPE values for the dissociation of the nitrogen molecule. ΔE are computed as the difference between the energies at equilibrium, $d = 1.078$ Å, and at $d = 3.0$ Å. The NPE values are given within parentheses. The results for HF, DFT, FCI, and CCSD are $\Delta E_{HF} = 1009.0$ (828.9) mHa, $\Delta E_{DFT} = 542.5$ (342.3) mHa, $\Delta E_{FCI} = 201.4$ (0.0) mHa, and $\Delta E_{CCSD} = -10.2$ (221.8) mHa, respectively. Situations that show an improvement of ΔE and the NPE compared to standard HF and DFT are highlighted in bold.

CAS	$\mu = 7.0$ (NPE)	HF-Emb. (NPE)	CASSCF (NPE)
(2, 4)	597.8 (417.8)	597.4 (416.5)	597.4 (416.9)
(4, 5)	431.8 (243.4)	432.8 (249.7)	441.9 (250.9)
(6, 6)	**180.8 (66.6)**	**172.5 (29.0)**	**186.7 (15.4)**
(8, 7)	**189.7 (16.4)**	**180.4 (21.1)**	**194.6 (6.8)**

TABLE III. Dissociation energies, ΔE, and NPE values for the dissociation of the oxygen molecule. ΔE are computed as the difference between the energies at equilibrium, d = 1.218 Å, and at d = 3.0 Å. The NPE values are given within parentheses. The results for HF, DFT, FCI, and CCSD are ΔE_{HF} = 687.9 (598.5) mHa, ΔE_{DFT} = 340.6 (202.8) mHa, ΔE_{FCI} = 138.3 (0.0) mHa, and ΔE_{CCSD} = 384.8 (248.2) mHa, respectively. Situations that show an improvement of ΔE and the NPE compared to standard HF and DFT are highlighted in bold.

CAS	μ = 8.0 (NPE)	HF-Emb. (NPE)	CASSCF (NPE)
(2, 3)	367.3 (338.0)	687.9 (598.5)	687.9 (598.5)
(4, 4)	93.1 (147.7)	365.5 (260.7)	54.8 (274.0)
(6, 5)	**135.2 (50.4)**	**138.9 (37.1)**	**143.5 (41.0)**
(8, 6)	**119.7 (18.6)**	**120.5 (17.9)**	**133.6 (4.8)**
(10, 7)	**124.8 (13.6)**	**125.3 (14.2)**	**136.8 (1.6)**

C. The dissociation of oxirane

As a final example, we consider the oxirane molecule, C_2H_4O, a system that is not possible to simulate with a brute force all-electron calculation with state-of-the-art quantum computers. In fact, the number of qubits and the required circuit depth for the representation of the system wavefunction would by far exceed the possibility of current hardware. On the other hand, we can show that by using DFT embedding with a suitable choice of the active space, we can achieve a sizable improvement of the energetics associated with the cleavage of the C–C bond in oxirane compared to standard DFT. Once more, due to the current limitation of our embedding schemes and the requirements for the calculation of the FCI reference, we limit the DFT calculation to the LDA functional and the basis set to STO-3G. The KS-MOs obtained under these conditions are presented in Fig. S13 of the supplementary material, and as previously encountered, Fig. 10 illustrates an energy diagram of this system.

Figure 11 depicts the dissociation profiles of oxirane between d = 1.0 Å and d = 3.0 Å for a selection of ASs. For the DFT embedding scheme, the analysis performed in the supplementary material (see Fig. S9) suggests an optimal range-separation parameter of μ_{opt} = 6.0. The overall behavior is similar to the one observed for the previous systems, suggesting that the scheme can be safely extended to larger systems. However, we expect that in order to achieve chemically accurate results, the use of better DFT functionals (beyond the simple LDA used here) for the description of the embedding potential will become of increasing importance. In addition, in this case, the accuracy of the dissociation profile increases smoothly with the size of the AS. Similarly, as for O_2, we also notice discontinuities between d = 2.75 Å and d = 3.0 Å for the DFT embedding CAS(2, 6) and the HF embedding CAS(6, 6) calculations due to the crossing of molecular orbital levels and the consequent changes in the composition of the AS.

Table IV summarizes the dissociation energies and NPEs for the profiles reported in Fig. 11. The values highlighted in bold corresponds to the best results achievable with the current implementation of the embedding schemes. As expected, due to the dimension

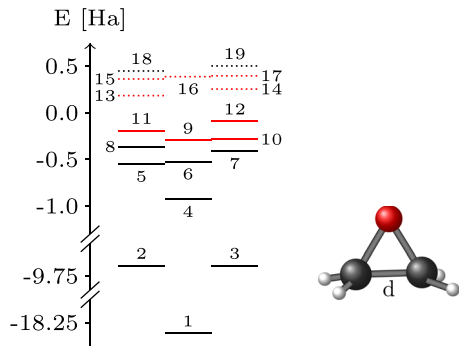

FIG. 10. Energy diagram of the KS-MOs of oxirane in the STO-3G basis. The solid lines correspond to occupied MOs, while the dotted lines represent virtual ones. In *red* are the orbitals involved in at least one of the ASs considered.

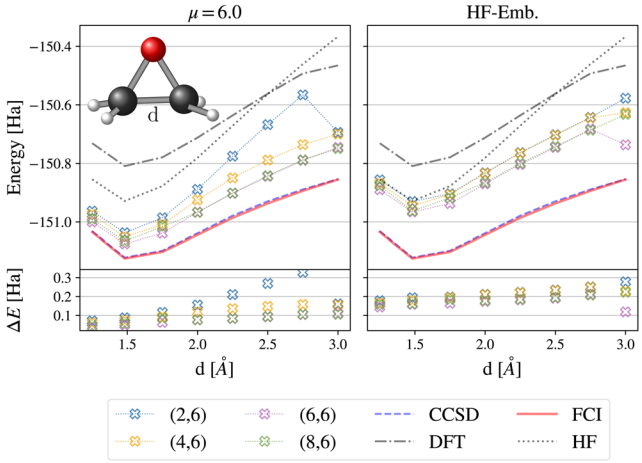

FIG. 11. (Upper panels) Dissociation profiles of an oxirane molecule in the STO-3G basis set. The left panel reports the energies obtained with the DFT embedding scheme at μ = 6.0, while the right panel shows the same curves obtained with the HF embedding scheme, respectively. The size of the ASs is reported in the legend with the format: (number of electrons, number of orbitals). The HF (gray, dotted), DFT (gray, dashed-dotted) (LDA/VWN XCF), CCSD (blue, dashed), and FCI (red, solid) references were computed with PySCF. The DFT reference line has been shifted by −0.3Ha to improve the scaling of the figure. (Lower panels) Energy differences with respect to the exact FCI reference.

TABLE IV. Dissociation energies, ΔE, and NPE values for the dissociation of the oxirane molecule. ΔE are computed as the difference between the energies at equilibrium, d = 1.482 Å, and at d = 3.0 Å. The NPE values are given within parentheses. The results for HF, DFT, FCI, and CCSD are ΔE_{HF} = 562.0 (308.8) mHa, ΔE_{DFT} = 343.9 (97.9) mHa, ΔE_{FCI} = 268.9 (0.0) mHa, and ΔE_{CCSD} = 267.4 (5.4) mHa, respectively. Situations that show an improvement of ΔE and the NPE compared to standard HF and DFT are highlighted in bold.

CAS	μ = 6.0 (NPE)	HF-Emb. (NPE)	CASSCF (NPE)
(2, 6)	343.1 (256.8)	352.9 (99.8)	345.9 (92.8)
(4, 6)	351.3 (97.8)	318.3 (82.8)	238.7 (112.5)
(6, 6)	**328.9 (75.5)**	**229.1 (93.0)**	**233.8 (35.1)**
(8, 6)	**316.2 (61.8)**	**330.1 (64.6)**	**263.2 (83.3)**

of the system (with 18 valence electrons) and the size of the larger active space [CAS(8, 6)], we cannot expect to achieve results comparable with FCI for both embedding schemes. However, we notice a sizable improvement of the HF embedding dissociation energies [from the HF value of 562.0 mHa to 229.1 mHa in CAS(6, 6)] and a smaller, but still significant, correction of about 60% in the DFT case. Further studies with more accurate DFT functionals will be needed to assess the potential of the DFT embedding in more complex systems.

V. CONCLUSIONS

In this work, we introduced an embedding scheme that enables the partitioning of electronic structure calculations into an Active Space (AS) subsystem treated with a high level quantum algorithm and an *environment* described at the HF or DFT level of theory. In this way, we can restrict the quantum calculations to a critical subset of molecular orbitals that can fit on state-of-the-art quantum computers, while the remaining electrons provide the embedding potential computed using a classical algorithm. Since for most chemical processes the quality of the electronic structure predictions depends on a small set of frontier orbitals, this scheme will allow the solution of interesting quantum chemistry problems where the AS can be described with a quantum algorithm presenting a favorable scaling in the number of active electrons. We demonstrate the performance of the embedding schemes in the case of the dissociation of a few test molecular systems, namely, molecular nitrogen, molecular oxygen, water, and oxirane, highlighting the benefits of the recursive update of the embedding potential to enhance the convergence of the ground state calculations. The improvements in accuracy obtained in the strongly correlated bond-breaking regime are significant in all tested systems and for both embedding schemes, demonstrating the potential of this approach. It is important to mention that the use of the iterative range-separated DFT embedding requires the tuning of an extra parameter, which cannot be set *a priori*. Further investigation is needed to automatize this technique for general use in larger molecular systems. Of particular relevance are the results obtained for oxirane, which demonstrate the applicability of the proposed quantum embedding scheme to complex organic molecules.

Improvements of the proposed embedding scheme can be obtained through the combination of the iterative update of the embedding potential with the simultaneous optimization of the active orbitals, as done, for instance, in the multiconfigurational self-consistent field (MCSCF) approach. We believe that the proposed HF and DFT embedding schemes will provide a fundamental framework for the scaling up of quantum electronic structure calculations to large molecular systems with an arbitrary number of electrons (i.e., as many as HF or DFT calculations can deal with).

The possibility of partitioning the solution of the electronic structure problem into an *active* component (defined by the AS) treated by means of a quantum computing algorithm and an *inert environment* component solved at the HF or DFT level of theory (as presented here and in other previous studies) will make it possible to use quantum computers in the solution of important problems in physics, chemistry, biology, and medicine.

SUPPLEMENTARY MATERIAL

The supplementary material reports on additional HF-embedding calculations obtained for larger basis sets as well as additional results obtained with different choices of the AS. Also provided are detailed plots for the selection of the range-separation parameters μ employed in our calculations and sketches of the MOs for all investigated systems, as well as, the atomic coordinates used in the calculations.

ACKNOWLEDGMENTS

The authors thank Valery Weber and Jürg Hutter for useful discussions as well as Manfred Sigrist who advised M.R. during a significant part of this work.

I.T., P.J.O., and M.R. acknowledge financial support from the Swiss National Science Foundation (SNF) through Grant No. 200021-179312.

APPENDIX A: HARTREE–FOCK EMBEDDING

In this section, we provide more detailed derivations of the HF embedding. First, we derive the restricted spin case and generalize the equations for unrestricted spins in the second part of this section.

1. Restricted spins

We introduce the splitting of the one-electron density matrix, $D = D^A + D^I$, into Eq. (1), one term at a time. The simplest case is the one of the one-electron contribution, which becomes

$$\begin{aligned}\sum_{pq} h_{pq} D_{pq} &= \sum_{vq} h_{vq} D^A_{vq} + \sum_{jq} h_{jq} D^I_{jq} \\ &= \sum_{uv} h_{uv} D^A_{uv} + 2\sum_{j} h_{jj},\end{aligned} \tag{A1}$$

where we use the fact that a density matrix element vanishes when any of its indices correspond to a virtual orbital. We can proceed analogously with the two-electron terms as in

$$\frac{1}{2}\sum_{pqrs} g_{pqrs} d_{pqrs} = \frac{1}{2}\sum_{pqjs} g_{pqjs} d_{pqjs} + \frac{1}{2}\sum_{jqus} g_{jqus} d_{jqus} + \frac{1}{2}\sum_{vqus} g_{vqus} d_{vqus}. \tag{A2}$$

We can now express the two-electron density matrices in terms of one-electron ones,

$$\begin{aligned} d_{pqjs} &= D_{pq} D_{js} - \delta_{qj} D_{ps} \\ &= 2\delta_{js} D_{pq} - \delta_{qj}\delta_{sq} D_{pq} \\ &= (2\delta_{js} - \delta_{qj}\delta_{sq}) D_{pq} \end{aligned} \tag{A3a}$$

and

$$\begin{aligned} d_{jqus} = d_{usjq} &= D_{us} D_{jq} - \delta_{sj} D_{uq} \\ &= 2\delta_{jq} D_{us} - \delta_{sj} D_{uq} \\ &= 2\delta_{qj}\delta_{sq} D_{uq} - \delta_{sj} D_{uq} \\ &= (2\delta_{qj}\delta_{sq} - \delta_{sj}) D_{uq}, \end{aligned} \tag{A3b}$$

where we omit the superscripts I and A for brevity. These expressions can then be inserted into Eq. (A2) to obtain

$$\frac{1}{2}\sum_{pqrs} g_{pqrs} d_{pqrs} = \sum_{pqj} g_{pqjj} D_{pq} - \frac{1}{2}\sum_{pqj} g_{pjjq} D_{pq} + \sum_{jqu} g_{jjuq} D^A_{uq} - \frac{1}{2}\sum_{jqu} g_{jquj} D^A_{uq} + \frac{1}{2}\sum_{uvxy} g_{uvxy} d^A_{uvxy}. \tag{A4}$$

Upon inspection, it becomes clear that the first two sums only yield non-zero contributions when $p = q = k$ or when $p = u$ and $q = v$. In the latter case, this causes the sums to coincide with the third and fourth terms. These observations allow us to simplify Eq. (A4) to become

$$\frac{1}{2}\sum_{pqrs} g_{pqrs} d_{pqrs} = 2\sum_{kj}\left(g_{kkjj} - \frac{1}{2} g_{kjjk}\right) + 2\sum_{jvu}\left(g_{jjuv} - \frac{1}{2} g_{jvuj}\right) D^A_{uv} + \frac{1}{2}\sum_{uvxy} g_{uvxy} d^A_{uvxy}. \tag{A5}$$

Finally, we can substitute Eqs. (A1) and (A5) into Eq. (1), yielding

$$E = \sum_j \left[2h_{jj} + \sum_k (2g_{kkjj} - g_{kjjk})\right] + \sum_{uv}\left[h_{uv} + \sum_j (2g_{jjuv} - g_{jvuj})\right] D^A_{uv} + \frac{1}{2}\sum_{uvxy} g_{uvxy} d^A_{uvxy}. \tag{A6}$$

This equation simplifies to Eq. (2) with the use of the *inactive Fock operator*, Eq. (3), and the *inactive energy*, Eq. (4).

2. Unrestricted spins

For unrestricted spins, we have to remove the implicit summation over the spin state, σ, and calculate with the one- and two-electron density matrices for each spin separately,

$$D^\sigma_{pq} = \langle \Psi | \hat{E}^\sigma_{pq} | \Psi \rangle \qquad \forall \sigma \in \{\alpha, \beta\}, \tag{A7a}$$

$$d^{\sigma\tau}_{pqrs} = \langle \Psi | \hat{e}^{\sigma\tau}_{pqrs} | \Psi \rangle \qquad \forall \sigma, \tau \in \{\alpha, \beta\}, \tag{A7b}$$

$$\hat{E}^\sigma_{pq} = \hat{a}^\dagger_{p\sigma} \hat{a}_{q\sigma} \qquad \forall \sigma \in \{\alpha, \beta\}, \tag{A7c}$$

$$\hat{e}^{\sigma\tau}_{pqrs} = \begin{cases} \hat{E}^\sigma_{pq}\hat{E}^\sigma_{rs} - \delta_{qr}\hat{E}^\sigma_{ps}, & \sigma = \tau \\ \hat{E}^\sigma_{pq}\hat{E}^\tau_{rs}, & \sigma \neq \tau \end{cases} \qquad \forall \sigma, \quad \tau \in \{\alpha, \beta\}. \tag{A7d}$$

Thus, in contrast to the closed shell description with restricted spins in Appendix A 1, we now have to keep track of the spin state where each index iterates over. This is indicated by the additional superscripts, σ and τ, and summation labels, n_σ and n_τ. For brevity, we refrain from explicitly denoting that $\sigma, \tau \in \{\alpha, \beta\}$ for the remainder of this derivation.

Analogous to Eq. (A1), the one-electron contribution can be written per spin state as

$$\sum_{pq}^{n_\sigma} h_{pq} D^\sigma_{pq} = \sum_{uv}^{n_\sigma} h_{uv} D^{A,\sigma}_{uv} + \sum_j^{n_\sigma} h_{jj}. \tag{A8}$$

For the two-electron contributions, we have to differentiate between two cases. In the first case, the spins of both electrons are aligned, $\sigma = \tau$, and the resulting equation can be derived in full analogy to Eq. (A5),

$$\frac{1}{2}\sum_{pq}^{n_\sigma}\sum_{rs}^{n_\sigma} g_{pqrs} d^{\sigma\sigma}_{pqrs} = \frac{1}{2}\sum_k^{n_\sigma}\sum_j^{n_\sigma}(g_{kkjj} - g_{kjjk}) + \sum_j^{n_\sigma}\sum_{uv}^{n_\sigma}(g_{jjuv} - g_{jvuj}) D^{A,\sigma}_{uv} + \frac{1}{2}\sum_{uv}^{n_\sigma}\sum_{xy}^{n_\sigma} g_{uvxy} d^{A,\sigma\sigma}_{uvxy}. \tag{A9}$$

The second case of opposite spins, $\sigma \neq \tau$, behaves slightly different due to the differing two-electron excitation operator, Eq. (A7d). Thus, the expression of the two-electron density matrices in terms of one-electron ones analogous to Eq. (A1) becomes

$$d^{\sigma\tau}_{pqjs} = D^\sigma_{pq} D^\tau_{js} = \delta_{js} D^\sigma_{pq} \tag{A10a}$$

and

$$d^{\sigma\tau}_{jqus} = D^\sigma_{jq} D^\tau_{us} = \delta_{jq} D^\tau_{us}, \tag{A10b}$$

which leads to the first expression of the two-electron contribution of opposite spins,

$$\frac{1}{2}\sum_{pq}^{n_\sigma}\sum_{rs}^{n_\tau} g_{pqrs} d^{\sigma\tau}_{pqrs} = \frac{1}{2}\sum_{pq}^{n_\sigma}\sum_j^{n_\tau} g_{pqjj} D^\sigma_{pq} + \frac{1}{2}\sum_j^{n_\sigma}\sum_{us}^{n_\tau} g_{jjus} D^{A,\tau}_{us} + \frac{1}{2}\sum_{vq}^{n_\sigma}\sum_{us}^{n_\tau} g_{vqus} d^{A,\sigma\tau}_{vqus}. \tag{A11}$$

Using the same arguments as before, we can once again simplify this equation to become

$$\frac{1}{2}\sum_{pq}^{n_\sigma}\sum_{rs}^{n_\tau} g_{pqrs} d^{\sigma\tau}_{pqrs} = \frac{1}{2}\sum_k^{n_\sigma}\sum_j^{n_\tau} g_{kkjj} + \frac{1}{2}\sum_{uv}^{n_\sigma}\sum_j^{n_\tau} g_{uvjj} D^{A,\sigma}_{uv} + \frac{1}{2}\sum_j^{n_\sigma}\sum_{uv}^{n_\tau} g_{jjuv} D^{A,\tau}_{uv} + \frac{1}{2}\sum_{uv}^{n_\sigma}\sum_{xy}^{n_\tau} g_{uvxy} d^{A,\sigma\tau}_{uvxy}. \tag{A12}$$

Finally, we can obtain the two-electron contributions for unrestricted spins by combining Eqs. (A9) and (A12) into

$$\begin{aligned}\frac{1}{2}\sum_{pqrs} g_{pqrs} d_{pqrs} = {} & \frac{1}{2}\sum_j^{n_\alpha}\left[\sum_k^{n_\alpha}(g_{kkjj} - g_{kjjk}) + \sum_k^{n_\beta} g_{kkjj}\right] \\ & + \frac{1}{2}\sum_j^{n_\beta}\left[\sum_k^{n_\beta}(g_{kkjj} - g_{kjjk}) + \sum_k^{n_\alpha} g_{kkjj}\right] \\ & + \sum_{uv}^{n_\alpha}\left[\sum_j^{n_\alpha}(g_{uvjj} - g_{ujjv}) + \sum_j^{n_\beta} g_{uvjj}\right] D^{A,\alpha}_{uv} \\ & + \sum_{uv}^{n_\beta}\left[\sum_j^{n_\beta}(g_{uvjj} - g_{ujjv}) + \sum_j^{n_\alpha} g_{uvjj}\right] D^{A,\beta}_{uv} \\ & + \frac{1}{2}\sum_{uvxy} g_{uvxy} d^A_{uvxy}.\end{aligned} \tag{A13}$$

In full analogy to the restricted spin case, this allows us to define the *inactive* Fock operator and energy as

$$F^{I,\sigma}_{pq} = h_{pq} + \sum_i^{n_\sigma}(g_{iipq} - g_{iqpi}) + \sum_i^{n_\tau} g_{iipq} \tag{A14}$$

and

$$E^I = \frac{1}{2}\sum_{\sigma=\alpha}^{\beta}\sum_j h_{jj} + F^{I,\sigma}_{jj} = \frac{1}{2}\sum_{\sigma=\alpha}^{\beta}\sum_{ij}(h_{ij} + F^{I,\sigma}_{ij}) D^{I,\sigma}_{ij}. \tag{A15}$$

APPENDIX B: DENSITY FUNCTIONAL THEORY EMBEDDING

In this appendix, we provide more detailed steps deriving the embedding equations of the iterative DFT embedding scheme. In doing so, we follow the work of Hedegård *et al.*[58] rather closely. We focus on the steps necessary to arrive at the final form of the total electronic energy, Eq. (15), after the introduction of the linear model, Eq. (13).

We start by noting that $\Delta D^{(i)}_{pq} = \Delta D^{A,(i)}_{uv}$ since the inactive part of the density matrix, D^I_{ij}, is constant by definition. Thus, we can express the total electronic energy after exploiting inherent properties of the one-electron density matrices as

$$E = E^{I,\mathrm{LR}} + E^{A,(i+1),\mathrm{LR}} + E^{\mathrm{SR}}_{\mathrm{coul+xc}}\left[\rho^{(i)}\right] + \sum_{uv}\left(j^{(i),\mathrm{SR}}_{uv} + v^{\mathrm{SR}}_{\mathrm{xc},uv}\left[\rho^{(i)}\right]\right)\Delta D^{A,(i)}_{uv}. \tag{B1}$$

To ease the implementation of Eq. (B1), we can rewrite the equation and group its terms into active and inactive ones. To do so, we start by rewriting the Coulomb part of the third term by expanding $D^{(i)} = D^I + D^{A,(i)}$ twice,

$$\begin{aligned} J^{\mathrm{SR}}\left[\rho^{(i)}\right] &= \frac{1}{2}\sum_{pqrs} D^{(i)}_{pq} g^{\mathrm{SR}}_{pqrs} D^{(i)}_{rs} \\ &= \frac{1}{2}\sum_{pq} D^{(i)}_{pq}\left(\sum_{ij} g^{\mathrm{SR}}_{pqij} D^I_{ij} + \sum_{uv} g^{\mathrm{SR}}_{pquv} D^{A,(i)}_{uv}\right) \\ &= \frac{1}{2}\left(\sum_{klij} D^I_{kl} g^{\mathrm{SR}}_{klij} D^I_{ij} + \sum_{xyij} D^{A,(i)}_{xy} g^{\mathrm{SR}}_{xyij} D^I_{ij} \right. \\ &\quad \left. + \sum_{kluv} D^I_{kl} g^{\mathrm{SR}}_{kluv} D^{A,(i)}_{uv} + \sum_{xyuv} D^{A,(i)}_{xy} g^{\mathrm{SR}}_{xyuv} D^{A,(i)}_{uv}\right). \end{aligned} \tag{B2}$$

We can proceed analogously with the Coulomb part of the fourth term,

$$\begin{aligned} \sum_{uv} j^{(i),\mathrm{SR}}_{uv} \Delta D^{A,(i)}_{uv} &= \sum_{pquv} D^{(i)}_{pq} g^{\mathrm{SR}}_{pquv}\left(D^{A,(i+1)}_{uv} - D^{A,(i)}_{uv}\right) \\ &= \sum_{ijuv} D^I_{ij} g^{\mathrm{SR}}_{ijuv} D^{A,(i+1)}_{uv} - D^I_{ij} g^{\mathrm{SR}}_{ijuv} D^{A,(i)}_{uv} \\ &\quad + \sum_{xyuv} D^{A,(i)}_{xy} g^{\mathrm{SR}}_{xyuv} D^{A,(i+1)}_{uv} - D^{A,(i)}_{xy} g^{\mathrm{SR}}_{xyuv} D^{A,(i)}_{uv}. \end{aligned} \tag{B3}$$

By gathering and canceling matching terms of Eqs. (B2) and (B3) through the use of the symmetry, $g_{pqrs} = g_{rspq}$, we arrive at the final expression of the SR Coulomb contributions,

$$\begin{aligned} J^{\mathrm{SR}}\left[\rho^{(i)}\right] + \sum_{uv} j^{(i),\mathrm{SR}}_{uv} \Delta D^{A,(i)}_{uv} &= \frac{1}{2}\sum_{ij} j^{I,\mathrm{SR}}_{ij} D^I_{ij} - \frac{1}{2}\sum_{uv} j^{A,(i),\mathrm{SR}}_{uv} D^{A,(i)}_{uv} \\ &\quad + \sum_{uv} j^{I,\mathrm{SR}}_{uv} D^{A,(i+1)}_{uv} + \sum_{uv} j^{A,(i),\mathrm{SR}}_{uv} D^{A,(i+1)}_{uv}. \end{aligned} \tag{B4}$$

Inserting Eq. (B4) into Eq. (B1) finally leads to

$$\begin{aligned} E &= E^{I,\mathrm{LR}} + E^{\mathrm{SR}}_{\mathrm{xc}}\left[\rho^{(i)}\right] + \frac{1}{2}\sum_{ij} j^{I,\mathrm{SR}}_{ij} D^I_{ij} \\ &\quad - \frac{1}{2}\sum_{uv} j^{A,(i),\mathrm{SR}}_{uv} D^{A,(i)}_{uv} - \sum_{uv} v^{\mathrm{SR}}_{\mathrm{xc},uv}\left[\rho^{(i)}\right] D^{A,(i)}_{uv} \\ &\quad + E^{A,\mathrm{LR}} + \sum_{uv} j^{I,\mathrm{SR}}_{uv} D^{A,(i+1)}_{uv} + \sum_{uv} j^{A,(i),\mathrm{SR}}_{uv} D^{A,(i+1)}_{uv} \\ &\quad + \sum_{uv} v^{\mathrm{SR}}_{\mathrm{xc},uv}\left[\rho^{(i)}\right] D^{A,(i+1)}_{uv}, \end{aligned} \tag{B5}$$

where we have re-ordered the terms such that the upper two lines contain all the inactive terms and the lower lines contain all the active ones. After insertion of the expressions for the LR energy contributions, E^I and E^A, according to Eqs. (4) and (2), respectively, we arrive at the final expression of the total electronic energy, Eq. (15).

The extension of these equations to unrestricted spins is similarly straight forward as in the case of the HF embedding (cf. Appendix A 2).

APPENDIX C: QISKIT'S EXCITATION OPERATOR ORDER IN THE q-UCCSD *ANSATZ*

In Qiskit, the order of the excitation operators of the q-UCCSD *Ansatz* is always constructed in a reproducible manner. For the purposes of this discussion, we assume that the number of electrons is stored as a pair in `nelec = (nalpha, nbeta)` and the number of spin orbitals accordingly in the pair `norbs`. Furthermore, we assume a *block*-ordering of the spin orbitals in the qubit register, meaning that the first half of the qubits maps to α-spin orbitals and the second half maps to β-spin orbitals.

With these assumptions in place, we can express Qiskit's order of excitation operators, as presented in Fig. 12. First, all α-spin

```
# alpha-spin single excitations
for qi in range(nelec[0]):
    for qj in range(nelec[0], norbs[0]):
        print('Single Excitation:',
              qi, '->', qj)

# beta-spin single excitations
for qk in range(norbs[0], nelec[1] + norbs[0]):
    for ql in range(nelec[1] + norbs[0],
                    norbs[1] + norbs[0]):
        print('Single Excitation:',
              qk, '->', ql)

# double excitations
for qi in range(nelec[0]):
    for qj in range(nelec[0], norbs[0]):
        for qk in range(norbs[0],
                        nelec[1] + norbs[0]):
            for ql in range(nelec[1] + norbs[0],
                            norbs[1] + norbs[0]):
                print('Double Excitation:',
                      qi, '->', qj, '&',
                      qk, '->', ql)
```

FIG. 12. A Python code outlining the order of the excitation operators of the q-UCCSD *Ansatz* as constructed in Qiskit.

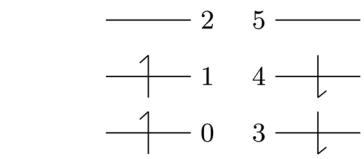


```
Single Excitation: 0 -> 2
Single Excitation: 1 -> 2
Single Excitation: 3 -> 5
Single Excitation: 4 -> 5
Double Excitation: 0 -> 2 & 3 -> 5
Double Excitation: 0 -> 2 & 4 -> 5
Double Excitation: 1 -> 2 & 3 -> 5
Double Excitation: 1 -> 2 & 4 -> 5
```

FIG. 13. Illustration of the ordering of the q-UCCSD excitations in Qiskit. (Top) Model system composed of four electrons in six orbitals [nelec = (2, 2) and norbs = (3, 3)]. (Bottom) Corresponding ordered list of excitations, as produced by the code in Fig. 12.

single-excitations are applied, followed by all β-spin ones. Then, all double-excitations are applied where the nested for loops are ordered such that the β-spin orbitals are iterated on the inner levels. To make this implementation more concrete, we present the output of the described code for the example of `nelec = (2, 2)` and `norbs = (3, 3)` in Fig. 13.

DATA AVAILABILITY

The data that support the findings of this study are available from the corresponding author upon reasonable request.

REFERENCES

[1] J. D. Whitfield, J. Biamonte, and A. Aspuru-Guzik, Mol. Phys. **109**, 735 (2011).
[2] T. Helgaker, S. Coriani, P. Jørgensen, K. Kristensen, J. Olsen, and K. Ruud, Chem. Rev. **112**, 543 (2012).
[3] K. D. Vogiatzis, M. V. Polynski, J. K. Kirkland, J. Townsend, A. Hashemi, C. Liu, and E. A. Pidko, Chem. Rev. **119**, 2453 (2018).
[4] M. Reiher, N. Wiebe, K. M. Svore, D. Wecker, and M. Troyer, Proc. Natl. Acad. Sci. U. S. A. **114**, 7555 (2017).
[5] M. Boero, M. Parrinello, and K. Terakura, J. Am. Chem. Soc. **120**, 2746 (1998).
[6] A. Aspuru-Guzik, R. Lindh, and M. Reiher, ACS Cent. Sci. **4**, 144 (2018).
[7] Y. Cao, J. Romero, and A. Aspuru-Guzik, IBM J. Res. Dev. **62**(6), 1 (2018).
[8] J.-M. Reiner, F. Wilhelm-Mauch, G. Schön, and M. Marthaler, Quantum Sci. Technol. **4**, 035005 (2019).
[9] I. O. Sokolov, P. K. Barkoutsos, P. J. Ollitrault, D. Greenberg, J. Rice, M. Pistoia, and I. Tavernelli, J. Chem. Phys. **152**, 124107 (2020).
[10] C. Kokail, C. Maier, R. van Bijnen, T. Brydges, M. K. Joshi, P. Jurcevic, C. A. Muschik, P. Silvi, R. Blatt, C. F. Roos, and P. Zoller, Nature **569**, 355 (2019).
[11] S. V. Mathis, G. Mazzola, and I. Tavernelli, "Toward scalable simulations of lattice gauge theories on quantum computers," Phys. Rev. D **102**, 094501 (2020).
[12] R. Babbush, N. Wiebe, J. McClean, J. McClain, H. Neven, and G. K.-L. Chan, Phys. Rev. X **8**, 011044 (2018).
[13] See https://quantum-computing.ibm.com/ for IBM, IBM Quantum Experience; accessed 16 March 2020.
[14] D. Wecker, M. B. Hastings, and M. Troyer, Phys. Rev. A **92**, 042303 (2015).
[15] A. Peruzzo, J. McClean, P. Shadbolt, M.-H. Yung, X.-Q. Zhou, P. J. Love, A. Aspuru-Guzik, and J. L. O'Brien, Nat. Commun. **5**, 4213 (2014).
[16] J. Čížek, J. Chem. Phys. **45**, 4256 (1966).
[17] H. G. Kümmel, "A biography of the coupled cluster method," in *Recent Progress in Many-Body Theories—Proceedings of the 11th International Conference*, edited by R. F. Bishop, T. Brandes, K. A. Gernoth, N. R. Walet, and Y. Xian (World Scientific Publishing, Singapore, 2002), pp. 334–348.
[18] R. J. Bartlett and M. Musiał, Rev. Mod. Phys. **79**, 291 (2007).
[19] P. J. J. O'Malley, R. Babbush, I. D. Kivlichan, J. Romero, J. McClean, R. Barends, J. Kelly, P. Roushan, A. Tranter, N. Ding, B. Campbell, Y. Chen, Z. Chen, B. Chiaro, A. Dunsworth, A. G. Fowler, E. Jeffrey, E. Lucero, A. Megrant, J. Y. Mutus, M. Neeley, C. Neill, C. Quintana, D. Sank, A. Vainsencher, J. Wenner, T. C. White, P. V. Coveney, P. J. Love, H. Neven, A. Aspuru-Guzik, and J. M. Martinis, Phys. Rev. X **6**, 031007 (2016).
[20] J. Romero, R. Babbush, J. R. McClean, C. Hempel, P. J. Love, and A. Aspuru-Guzik, Quantum Sci. Technol. **4**, 014008 (2018).
[21] P. K. Barkoutsos, J. F. Gonthier, I. Sokolov, N. Moll, G. Salis, A. Fuhrer, M. Ganzhorn, D. J. Egger, M. Troyer, A. Mezzacapo, S. Filipp, and I. Tavernelli, Phys. Rev. A **98**, 022322 (2018).
[22] N. Moll, P. Barkoutsos, L. S. Bishop, J. M. Chow, A. Cross, D. J. Egger, S. Filipp, A. Fuhrer, J. M. Gambetta, M. Ganzhorn, A. Kandala, A. Mezzacapo, P. Müller, W. Riess, G. Salis, J. Smolin, I. Tavernelli, and K. Temme, Quantum Sci. Technol. **3**, 030503 (2018).
[23] M. Kühn, S. Zanker, P. Deglmann, M. Marthaler, and H. Weiss, J. Chem. Theory Comput. **15**, 4764 (2019).
[24] N. P. Bauman, E. J. Bylaska, S. Krishnamoorthy, G. H. Low, N. Wiebe, C. E. Granade, M. Roetteler, M. Troyer, and K. Kowalski, J. Chem. Phys. **151**, 014107 (2019).
[25] F. A. Evangelista, G. K.-L. Chan, and G. E. Scuseria, J. Chem. Phys. **151**, 244112 (2019).
[26] W. Mizukami, K. Mitarai, Y. O. Nakagawa, T. Yamamoto, T. Yan, and Y-y. Ohnishi, "Orbital optimized unitary coupled cluster theory for quantum computer," Phys. Rev. Research **2**, 033421 (2019).
[27] A. F. Izmaylov, M. Díaz-Tinoco, and R. A. Lang, Phys. Chem. Chem. Phys. **22**, 12980 (2020).
[28] A. Kandala, A. Mezzacapo, K. Temme, M. Takita, M. Brink, J. M. Chow, and J. M. Gambetta, Nature **549**, 242 (2017).
[29] M. Ganzhorn, D. Egger, P. Barkoutsos, P. Ollitrault, G. Salis, N. Moll, M. Roth, A. Fuhrer, P. Mueller, S. Woerner, I. Tavernelli, and S. Filipp, Phys. Rev. Appl. **11**, 044092 (2019).
[30] I. G. Ryabinkin, T.-C. Yen, S. N. Genin, and A. F. Izmaylov, J. Chem. Theory Comput. **14**, 6317 (2018).
[31] I. G. Ryabinkin, R. A. Lang, S. N. Genin, and A. F. Izmaylov, J. Chem. Theory Comput. **16**, 1055 (2020).
[32] C. Hempel, C. Maier, J. Romero, J. McClean, T. Monz, H. Shen, P. Jurcevic, B. P. Lanyon, P. Love, R. Babbush, A. Aspuru-Guzik, R. Blatt, and C. F. Roos, Phys. Rev. X **8**, 031022 (2018).
[33] R. Sagastizabal, X. Bonet-Monroig, M. Singh, M. A. Rol, C. C. Bultink, X. Fu, C. H. Price, V. P. Ostroukh, N. Muthusubramanian, A. Bruno, M. Beekman, N. Haider, T. E. O'Brien, and L. DiCarlo, Phys. Rev. A **100**, 010302 (2019).
[34] F. Arute, K. Arya, R. Babbush, D. Bacon, J. C. Bardin, R. Barends, S. Boixo, M. Broughton, B. B. Buckley, D. A. Buell, B. Burkett, N. Bushnell, Y. Chen, Z. Chen, B. Chiaro, R. Collins, W. Courtney, S. Demura, A. Dunsworth, D. Eppens, E. Farhi, A. Fowler, B. Foxen, C. Gidney, M. Giustina, R. Graff, S. Habegger, M. P. Harrigan, A. Ho, S. Hong, T. Huang, W. J. Huggins, L. Ioffe, S. V. Isakov, E. Jeffrey, Z. Jiang, C. Jones, D. Kafri, K. Kechedzhi, J. Kelly, S. Kim, P. V. Klimov, A. Korotkov, F. Kostritsa, D. Landhuis, P. Laptev, M. Lindmark, E. Lucero, O. Martin, J. M. Martinis, J. R. McClean, M. McEwen, A. Megrant, X. Mi, M. Mohseni, W. Mruczkiewicz, J. Mutus, O. Naaman, M. Neeley, C. Neill, H. Neven, M. Y. Niu, T. E. O'Brien, E. Ostby, A. Petukhov, H. Putterman, C. Quintana, P. Roushan, N. C. Rubin, D. Sank, K. J. Satzinger, V. Smelyanskiy, D. Strain, K. J. Sung, M. Szalay, T. Y. Takeshita, A. Vainsencher, T. White, N. Wiebe, Z. J. Yao, P. Yeh, and A. Zalcman, "Hartree-Fock on a superconducting qubit quantum computer," Science **369**, 1084 (2020).

[35]P. J. Ollitrault, A. Kandala, C.-F. Chen, P. K. Barkoutsos, A. Mezzacapo, M. Pistoia, S. Sheldon, S. Woerner, J. M. Gambetta, and I. Tavernelli, Phys. Rev. Res. **2**, 043140 (2020).
[36]O. Higgott, D. Wang, and S. Brierley, Quantum **3**, 156 (2019).
[37]R. M. Parrish, E. G. Hohenstein, P. L. McMahon, and T. J. Martínez, Phys. Rev. Lett. **122**, 230401 (2019).
[38]K. M. Nakanishi, K. Mitarai, and K. Fujii, Phys. Rev. Res. **1**, 033062 (2019).
[39]I. G. Ryabinkin, S. N. Genin, and A. F. Izmaylov, J. Chem. Theory Comput. **15**, 249 (2018).
[40]J. R. McClean, M. E. Kimchi-Schwartz, J. Carter, and W. A. de Jong, Phys. Rev. A **95**, 042308 (2017).
[41]N. H. Stair, R. Huang, and F. A. Evangelista, J. Chem. Theory Comput. **16**, 2236 (2020).
[42]R. Santagati, J. Wang, A. A. Gentile, S. Paesani, N. Wiebe, J. R. McClean, S. Morley-Short, P. J. Shadbolt, D. Bonneau, J. W. Silverstone *et al.*, Sci. Adv. **4**, eaap9646 (2018).
[43]T. Jones, S. Endo, S. McArdle, X. Yuan, and S. C. Benjamin, Phys. Rev. A **99**, 062304 (2019).
[44]J. Tilly, G. Jones, H. Chen, L. Wossnig, and E. Grant, "Computation of molecular excited states on IBMQ using a discriminative variational quantum eigensolver," Phys. Rev. A **102**, 062425 (2020).
[45]B. O. Roos, P. R. Taylor, and P. E. M. Sigbahn, Chem. Phys. **48**, 157 (1980).
[46]T. Helgaker, P. Jèrgensen, and J. Olsen, *Molecular Electronic-Structure Theory* (John Wiley & Sons, Ltd., 2000).
[47]B. Bauer, D. Wecker, A. J. Millis, M. B. Hastings, and M. Troyer, Phys. Rev. X **6**, 031045 (2016).
[48]N. C. Rubin, "A hybrid classical/quantum approach for large-scale studies of quantum systems with density matrix embedding theory," arXiv:1610.06910v2 (2016).
[49]A. Georges and G. Kotliar, Phys. Rev. B **45**, 6479 (1992).
[50]G. Knizia and G. K.-L. Chan, Phys. Rev. Lett. **109**, 186404 (2012).
[51]X. Wu, M. Lindsey, T. Zhou, Y. Tong, and L. Lin, "Enhancing robustness and efficiency of density matrix embedding theory via semidefinite programming and local correlation potential fitting," Phys. Rev. B **102**, 085123 (2020).
[52]H. Ma, M. Govoni, and G. Galli, npj Comput. Mater. **6**, 85 (2020).
[53]A. Savin and H.-J. Flad, Int. J. Quantum Chem. **56**, 327 (1995).
[54]T. Takeshita, N. C. Rubin, Z. Jiang, E. Lee, R. Babbush, and J. R. McClean, Phys. Rev. X **10**, 011004 (2020).
[55]M. Urbanek, D. Camps, R. V. Beeumen, and W. A. de Jong, "Chemistry on quantum computers with virtual quantum subspace expansion," J. Chem. Theory Comput. **16**, 5425–5431 (2020).
[56]G. Aleksandrowicz, T. Alexander, P. Barkoutsos, L. Bello, Y. Ben-Haim, D. Bucher, F. J. Cabrera-Hernandez, J. Carballo-Franquis, A. Chen, C.-F. Chen, J. M. Chow, A. D. Corcoles-Gonzales, A. J. Cross, A. Cross, J. Cruz-Benito, C. Culver, S. D. L. P. Gonzalez, E. D. L. Torre, D. Ding, E. Dumitrescu, I. Duran, P. Eendebak, M. Everitt, I. F. Sertage, A. Frisch, A. Fuhrer, J. Gacon, J. Gambetta, B. G. Gago, J. Gomez-Mosquera, D. Greenberg, I. Hamamura, V. Havlicek, J. Hellmers, L. Herok, H. Horii, S. Hu, T. Imamichi, T. Itoko, A. Javadi-Abhari, N. Kanazawa, A. Karazeev, K. Krsulich, P. Liu, Y. Luh, Y. Maeng, M. Marques, F. J. Martin-Fernandez, D. T. McClure, D. McKay, S. Meesala, A. Mezzacapo, N. Moll, D. M. Rodriguez, G. Nannicini, P. Nation, P. J. Ollitrault, L. J. O'Riordan, H. Paik, J. Perez, A. Phan, M. Pistoia, V. Prutyanov, M. Reuter, J. Rice, A. R. Davila, M. Rossmannek, R. H. P. Rudy, M. Ryu, N. Sathaye, C. Schnabel, E. Schoute, K. Setia, Y. Shi, A. Silva, Y. Siraichi, S. Sivarajah, J. A. Smolin, M. Soeken, I. Sokolov, H. Takahashi, I. Tavernelli, C. Taylor, P. Taylour, K. Trabing, M. Treinish, W. Turner, D. Vogt-Lee, C. Vuillot, J. A. Wildstrom, J. Wilson, E. Winston, C. Wood, S. Wood, S. Wörner, I. Y. Akhalwaya, and C. Zoufal (2019). "Qiskit: An open-source framework for quantum computing," Zenodo. https://doi.org/10.5281/zenodo.2562111.
[57]S. B. Bravyi and A. Y. Kitaev, Ann. Phys. **298**, 210 (2002).
[58]E. D. Hedegård, S. Knecht, J. S. Kielberg, H. J. A. Jensen, and M. Reiher, J. Chem. Phys. **142**, 224108 (2015).
[59]See https://github.com/Qiskit/qiskit-nature/ for Qiskit, Qiskit Nature; accessed 29 January 2021.
[60]Q. Sun, J. Yang, and G. K.-L. Chan, Chem. Phys. Lett. **683**, 291 (2017).
[61]S. Bravyi, J. M. Gambetta, A. Mezzacapo, and K. Temme, "Tapering off qubits to simulate fermionic Hamiltonians," arXiv:1701.08213v1 (2017).
[62]J. L. Morales and J. Nocedal, ACM Trans. Math. Software **38**, 1 (2011).
[63]J. Toulouse, A. Savin, and H.-J. Flad, Int. J. Quantum Chem. **100**, 1047 (2004).
[64]S. Paziani, S. Moroni, P. Gori-Giorgi, and G. B. Bachelet, Phys. Rev. B **73**, 155111 (2006).
[65]U. Ekström, L. Visscher, R. Bast, A. J. Thorvaldsen, and K. Ruud, J. Chem. Theory Comput. **6**, 1971 (2010).
[66]J. Heyd, G. E. Scuseria, and M. Ernzerhof, J. Chem. Phys. **118**, 8207 (2003).
[67]E. Fromager, J. Toulouse, and H. J. A. Jensen, J. Chem. Phys. **126**, 074111 (2007).
[68]W. J. Hehre, R. F. Stewart, and J. A. Pople, J. Chem. Phys. **51**, 2657 (1969).
[69]P. C. Hariharan and J. A. Pople, Theor. Chim. Acta **28**, 213 (1973).
[70]T. H. Dunning, J. Chem. Phys. **90**, 1007 (1989).
[71]V. Veryazov, P. Å. Malmqvist, and B. O. Roos, Int. J. Quantum Chem. **111**, 3329 (2011).
[72]C. J. Stein and M. Reiher, J. Chem. Theory Comput. **12**, 1760 (2016).
[73]C. J. Stein and M. Reiher, J. Comput. Chem. **40**, 2216 (2019).
[74]F. M. Faulstich, M. Máté, A. Laestadius, M. A. Csirik, L. Veis, A. Antalik, J. Brabec, R. Schneider, J. Pittner, S. Kvaal, and Ö. Legeza, J. Chem. Theory Comput. **15**, 2206 (2019).
[75]E. R. Sayfutyarova, Q. Sun, G. K.-L. Chan, and G. Knizia, J. Chem. Theory Comput. **13**, 4063 (2017).
[76]X. Li and J. Paldus, J. Chem. Phys. **103**, 1024 (1995).